Combining Real Space and Tight Binding Methods for Studying Large Metallic Systems

C. Cornea and D. Stoeffler

Institut de Physique et Chimie des Matériaux de Strasbourg (CNRS UMR 7504),
Groupe d'Etude des Matériaux Métalliques,
23, rue du Loess, F-67037 Strasbourg, France

Abstract. In this paper some problems experienced during studies combining real space and tight binding methods are addressed. These methods have been mainly used for studying the magnetic properties of thin films deposited on substrates and of multilayers taking into account interfacial imperfections. This paper is illustrated with calculations of the electronic structure of Fe/Cr multilayered systems which are particularly interesting. First, the use of *d* and *spd* tight binding parameterisations of the electronic structure for transition metals and its relation to the recursion technique is discussed. Second, some advantages of using real space cells for studying complex systems are presented. Finally, the application of these methods for systems presenting non-collinear magnetism is discussed.

1 Introduction

During the last ten years, the electronic structure of large and complex metallic systems has been extensively studied mainly due to the enhancement of the computer facilities. Powerful computers with large memories became available allowing to reach rapidly self consistency in the band structure calculations for cells containing up to a few hundred of heavy atoms. One of these kinds of systems, concerns the metallic multilayers presenting new magnetic properties like the Interlayer Magnetic Coupling (IMC) or the Giant Magneto Resistance (GMR) effect particularly interesting for applications. This paper deals with the use of the real space recursion technique for the study of the magnetic order in such metallic multilayers.

The multilayered A_mB_n system built by alternating a m monolayers thick A layer with a n monolayers thick B layer consists in a long elemental chemical cell containing, in the simplest case, one non equivalent atom in the in plane cell and $m + n$ atoms in the growth direction perpendicular to the plane of the layers. Because these multilayers are periodic in the 3 directions of space, the band structure is usually calculated in the $\mathbf{k}$ space of the reciprocal lattice. However, since the aim of more complete studies is usually to determine the magnetic properties for thin overlayers during the growth of the multilayer, to include interfacial imperfections, to relate the growth mode and the magnetic behaviour, ... a real space technique is used in order to have the possibility to calculate the electronic structure of all these situations with the same method.

The aim of this paper is to discuss possible problems and solutions used

H. Dreyssé (Ed.): Workshop 1998, LNP 535, pp. 434–458, 1999.
© Springer-Verlag Berlin Heidelberg 1999

during various studies of the Fe/Cr multilayered system. A *d* restricted tight binding modelling of the band structure has been first used mainly because it needs less computer time than a full *spd* description and allows to use an exact cluster for the recursion technique. More recently, due to physical lacks in some results, the description has been extended taking the *spd* hybridisation into account. However, in order to reduce the computer time, clusters smaller than the exact one are used for the calculation. In the first section, some possible choices for the shape of these "inexact" clusters are given and their use for large cells like the one of multilayers is discussed. In the second section, the advantages of using real space cells for studying such complex systems are discussed. Finally, in the last section, the application of these methods for systems presenting non-collinear magnetism is presented.

2 Tight Binding Parameterisation and Recursion Technique

2.1 The Recursion Technique

This method, proposed by Haydock and Heine [1–3], is well suited for the determination of the electronic structure when (i) the Hamiltonian H can be expressed in a finite basis of localized orbital $|i,\lambda\rangle$ of symmetry λ on the site i (like the one considered in the next subsection) and (ii) when the knowledge of the Green function $G_{i,\lambda}(z) = \langle i,\lambda|G(z)|i,\lambda\rangle = \langle i,\lambda|(z-H)^{-1}|i,\lambda\rangle$ elements is sufficient for the calculation of the band structure. For example, this method applies to situations presenting no symmetry like amorphous or disordered systems, around impurities or structural imperfections.

For each given site and symmetry (i,λ), a new basis $|n\}$ is built in order to have a tridiagonal matrix for the representation of H in this new basis. The basis $|n\}$ is recursively obtained starting from the $|i,\lambda\rangle$ basis function with the following expressions:

$$\begin{aligned} |0\} &= |i,\lambda\rangle \\ |1\} &= H|0\} - a_1^{i,\lambda}|0\} \\ |n+1\} &= H|n\} - a_{n+1}^{i,\lambda}|n\} - b_n^{i,\lambda}|n-1\}. \end{aligned} \tag{1}$$

The sets $(a_n^{i,\lambda}, b_n^{i,\lambda})$ are called the recursion coefficients. They are easily obtained by calculations of simple scalar products:

$$\begin{aligned} a_{n+1}^{i,\lambda} &= \frac{\{n|H|n\}}{\{n|n\}} \\ b_{n+1}^{i,\lambda} &= \frac{\{n|H|n+1\}}{\{n|n\}} = \frac{\{n+1|n+1\}}{\{n|n\}}. \end{aligned} \tag{2}$$

The orthonormalized recursion basis is then obtained by:

$$|n\rangle = \frac{|n\}}{\sqrt{\{n|n\}}} \tag{3}$$

and the recursion coefficients correspond to:

$$\begin{aligned} a_{n+1}^{i,\lambda} &= \langle n|H|n\rangle \\ \sqrt{b_{n+1}^{i,\lambda}} &= \langle n|H|n+1\rangle = \langle n+1|H|n\rangle. \end{aligned} \tag{4}$$

The desired tridiagonal matrix representation of H is consequently obtained:

$$H = \begin{pmatrix} a_1^{i,\lambda} & \sqrt{b_1^{i,\lambda}} & & 0 \\ \sqrt{b_1^{i,\lambda}} & a_2^{i,\lambda} & \sqrt{b_2^{i,\lambda}} & \\ & \sqrt{b_2^{i,\lambda}} & a_3^{i,\lambda} & \sqrt{b_3^{i,\lambda}} \\ & & \sqrt{b_3^{i,\lambda}} & a_4^{i,\lambda} & \ddots \\ 0 & & & \ddots & \ddots \end{pmatrix}. \tag{5}$$

Since $|i,\lambda\rangle = |0\rangle$, the Green function $G_{i,\lambda}(z)$ is equal to $\langle 0|(z-H)^{-1}|0\rangle$ which corresponds to the first element $[(z-H)^{-1}]_{00}$ of the inverse matrix of $(z-H)$. This particular element is easily obtained by considering the determinants $\det(z-H_n) = ||z-H_n||$ where H_n is the part of the H matrix limited to the elements $\{|n\rangle, |n+1\rangle, |n+2\rangle, ...\}$ of the recursion basis,

$$H_n = \begin{pmatrix} a_{n+1}^{i,\lambda} & \sqrt{b_{n+1}^{i,\lambda}} & & 0 \\ \sqrt{b_{n+1}^{i,\lambda}} & a_{n+2}^{i,\lambda} & \sqrt{b_{n+2}^{i,\lambda}} & \\ & \sqrt{b_{n+2}^{i,\lambda}} & a_{n+3}^{i,\lambda} & \sqrt{b_{n+3}^{i,\lambda}} \\ & & \sqrt{b_{n+3}^{i,\lambda}} & a_{n+4}^{i,\lambda} & \ddots \\ 0 & & & \ddots & \ddots \end{pmatrix}. \tag{6}$$

The desired Green function is then equal to

$$\begin{aligned} G_{i,\lambda}(z) &= \frac{||z-H_1||}{||z-H_0||} \\ &= \frac{||z-H_1||}{(z-a_1^{i,\lambda})||z-H_1|| - b_1^{i,\lambda}||z-H_2||} \\ &= \frac{1}{z-a_1^{i,\lambda} - b_1^{i,\lambda}\frac{||z-H_2||}{||z-H_1||}} \end{aligned} \tag{7}$$

corresponding to the continuous fraction expansion

$$G_{i,\lambda}(z) = \cfrac{1}{z-a_1^{i,\lambda} - \cfrac{b_1^{i,\lambda}}{z-a_2^{i,\lambda} - \cfrac{b_2^{i,\lambda}}{z-a_3^{i,\lambda} - \cfrac{b_3^{i,\lambda}}{z-a_4^{i,\lambda} - \cfrac{b_4^{i,\lambda}}{\ddots}}}}}. \tag{8}$$

An analytical expression of the Green function is then obtained. However, an exact determination of $G_{i,\lambda}(z)$ requires an infinite number of recursion coefficients which is never the case in practical calculations. Usually, only a few levels (N pairs of (a_n, b_n) coefficients) of the continuous fraction are determined and the missing part of the fraction expansion is replaced by a terminator function $\Sigma_{i,\lambda}(z)$. The continuous fraction expansion becomes

$$G_{i,\lambda}(z) = \cfrac{1}{z - a_1^{i,\lambda} - \cfrac{b_1^{i,\lambda}}{z - a_2^{i,\lambda} - \cfrac{b_2^{i,\lambda}}{z - a_3^{i,\lambda} - \cfrac{b_3^{i,\lambda}}{\ddots \cfrac{}{z - a_N^{i,\lambda} - \cfrac{b_N^{i,\lambda}}{\Sigma_{i,\lambda}(z)}}}}}}. \tag{9}$$

For energy bands presenting no gap, the recursion coefficients have asymptotic limits corresponding to $(a_\infty^{i,\lambda}, b_\infty^{i,\lambda})$. The most easy way to determine $\Sigma_{i,\lambda}(z)$ is to assume that for $n > N$ the recursion coefficients are equal to their asymptotic values. The terminator function is then equal to:

$$\begin{aligned}\Sigma_{i,\lambda}(z) &= z - a_\infty^{i,\lambda} - \cfrac{b_\infty^{i,\lambda}}{z - a_\infty^{i,\lambda} - \cfrac{b_\infty^{i,\lambda}}{z - a_\infty^{i,\lambda} - \cfrac{b_\infty^{i,\lambda}}{\ddots}}} \\ &= z - a_\infty^{i,\lambda} - \frac{b_\infty^{i,\lambda}}{\Sigma_{i,\lambda}(z)}.\end{aligned} \tag{10}$$

The solution of this equation gives the square root expression of the terminator function:

$$\Sigma_{i,\lambda}(z) = \frac{z - a_\infty^{i,\lambda} \pm \sqrt{(z - a_\infty^{i,\lambda})^2 - 4b_\infty^{i,\lambda}}}{2}. \tag{11}$$

The Beer-Pettifor method is used [4] to determine $(a_\infty^{i,\lambda}, b_\infty^{i,\lambda})$ which is based on the calculation of the band limits $(\epsilon_{\min}, \epsilon_{\max})$ given by $(a_\infty^{i,\lambda} - 2\sqrt{b_\infty^{i,\lambda}}, a_\infty^{i,\lambda} + 2\sqrt{b_\infty^{i,\lambda}})$. When the continuous fraction is truncated at the level N, the projected density of states (PDOS)

$$n_{i,\lambda}(\epsilon) = -\frac{1}{\pi}\mathrm{Im}(G_{i,\lambda}(\epsilon + i0)) \tag{12}$$

corresponds to a sum of Dirac functions and the band limits can be identified by the energies of the lowest and highest Dirac functions. This method is extremely easy to use and, because it needs only to determine the diagonal representation of relatively small matrices, is also rapid and numerically stable. However, because the band limits correspond to Dirac functions, using the exact values obtained by this method gives usually diverging values for the PDOS near the band limits. Since the band width is underestimated by this method (due to the truncation

of the continuous fraction), this problem can be nicely solved by enlarging the calculated band by 1%. One way to check the efficiency of this method for the determination of the terminator function is to verify that the PDOS are correctly normalized which is usually the case with an error smaller that 10^{-5}.

For each level of the recursion calculation (2), the hamiltonian H is applied on the n-th element $|n\}$ of the new basis. This adds to the expression of $|n+1\}$ all new "neighbours" linked through H of all sites included in the expression of $|n\}$. In other words, at each level of the recursion calculation, the contribution of the n-th shell of "neighbours" of the starting site $|i,\lambda\rangle$ is taken into account. Consequently, the number of sites needed for calculating N exact levels of the continuous fraction (or N exact pairs of recursion coefficients) is proportional to N^3 [5].

2.2 Tight Binding Hamiltonian

In the Linear Combination of Atomic Orbitals method, the one-electron wave function $|\Psi\rangle$ is expressed as a linear combination of localized atomic orbital $|i,\lambda\rangle$ on site i and spin-symmetry λ:

$$|\Psi\rangle = \sum_{i,\lambda} c_{i,\lambda}|i,\lambda\rangle. \tag{13}$$

Solving Schroedinger equation becomes the eigen-value problem

$$\begin{aligned} \sum_{i,\lambda} c_{i,\lambda}(\langle j,\mu|H|i,\lambda\rangle - \epsilon\langle j,\mu|i,\lambda\rangle) &= 0 \\ \sum_{i,\lambda} c_{i,\lambda}(H_{i,j}^{\lambda,\mu} - \epsilon S_{i,j}^{\lambda,\mu}) &= 0. \end{aligned} \tag{14}$$

The overlap matrix $S_{i,j}^{\lambda,\mu}$ plays an essential role when the atomic orbital can not be assumed as being orthogonal [6]. In this work, it is assumed that S is equal to identity $S_{i,j}^{\lambda,\mu} = \delta_{i,j}\delta_{\lambda,\mu}$. The hamiltonian can then be directly expressed in the atomic orbital basis

$$H = \sum_{(i,\lambda),(j,\mu)} |j,\mu\rangle H_{i,j}^{\lambda,\mu}\langle i,\lambda| \tag{15}$$

which can be split into intrasite and intersite terms

$$H = \sum_{i,\lambda,\mu} |i,\mu\rangle\epsilon_{i,\lambda,\mu}\langle i,\lambda| + \sum_{(i,\lambda),(j\neq i,\mu)} |j,\mu\rangle\beta_{i,j}^{\lambda,\mu}\langle i,\lambda|. \tag{16}$$

$\epsilon_{i,\lambda,\mu}$ are the on-site energy levels and $\beta_{i,j}^{\lambda,\mu}$ are the two-center hopping integrals linking sites i and j. In order to reduce the numbers of parameters of the hamiltonian, the on-site energy levels are assumed to be equal to

$$\epsilon_{i,\lambda,\mu} = \left(\epsilon_{i,\lambda}^0 + U_{i,l(\lambda)}\Delta N_{i,l(\lambda)} + \sigma_\lambda \frac{I_{i,l(\lambda)}M_{i,l(\lambda)}}{2}\right)\delta_{\lambda,\mu} \tag{17}$$

where $\epsilon^0_{i,\lambda}$, $U_{i,l(\lambda)}$, $\Delta N_{i,l(\lambda)}$ and $I_{i,l(\lambda)}$ are respectively the spin independent energy level reference, the effective Coulomb integral, the charge variation and the effective Exchange integral of site i, $M_{i,l(\lambda)}$ is the local magnetic moment, $l(\lambda)$ and σ_λ being respectively the orbital quantum number (corresponding to s, p or d states) and the spin of the spin-symmetry λ. The charge variation $\Delta N_{i,l(\lambda)}$ and the local magnetic moment $M_{i,l(\lambda)}$ are obtained from the PDOS by

$$\Delta N_{i,l} = \sum_\lambda \delta_{l(\lambda),l} \int^{\epsilon_F} n_{i,\lambda}(\epsilon) d\epsilon - N^0_{i,l} \tag{18}$$

where $N^0_{i,l}$ is the bulk l band occupation of site i and

$$M_{i,l} = \sum_\lambda \delta_{l(\lambda),l} \int^{\epsilon_F} (\delta_{\sigma_\lambda,+} n_{i,\lambda}(\epsilon) - \delta_{\sigma_\lambda,-} n_{i,\lambda}(\epsilon)) d\epsilon \tag{19}$$

Equations (17), (18) and (19) define the self consistency solution. The input charge variations and magnetic moments allow to calculate the input energy levels of the hamiltonian for which the output PDOS are determined and integrated to obtain the output charge variations and magnetic moments. Self consistency is reached when input and output quantities do not more differ significantly.

Usually, four energy levels ϵ^0_s, ϵ^0_p, $\epsilon^0_{E_g}$ and $\epsilon^0_{T_{2g}}$ are needed for each site and the hopping integrals $\beta^{\lambda,\mu}_{i,j}$ between each pair of sites are expressed in terms of ten simple Slater-Koster matrix elements [7] $ss\sigma$, $sp\sigma$, $sd\sigma$, $pp\sigma$, $pp\pi$, $pd\sigma$, $pd\pi$, $dd\sigma$, $dd\pi$ and $dd\delta$. It has been shown that a good description of the band structure can be obtained by limiting the hopping integrals to nearest neighbours pairs of sites. Various sets of hopping integrals for a given element can be found in the literature showing that the Slater-Koster matrix elements do not have an unique value [8].

As an illustration, the density of states (DOS) obtained using the Slater-Koster parameters deduced by fitting *ab initio* band structure calculations by Papaconstantopoulos [9] and those obtained using the TB-LMTO method by Andersen *et al* [10] are compared. Fig. 1 shows the DOS obtained for bulk non magnetic Chromium using these two sets of parameters. The d bands are very similar for both calculations. For the s and p DOS, if the bottom of the bands for both calculations are very similar, the DOS differ significantly for higher energies (larger than 15 eV). Due to the finite band width of tight binding DOS, the band structure shows non physical structures at high energies for all sets of parameters. However, with tight binding parameters taken from Papaconstantopoulos, the total band width (W) is approximately equal to 45 eV whereas with the second set of parameters W is approximately equal to 25 eV. Since the energy resolution of the DOS calculated with the recursion method is proportionnal to W divided by the number of levels, the larger W is, the smaller the energy resolution of the DOS - for a same number of recursion levels - is. Consequently, the d DOS - which is the most important for itinerant magnetism properties - exhibits more fine structures when W is smaller (Fig. 1.b) than for the other

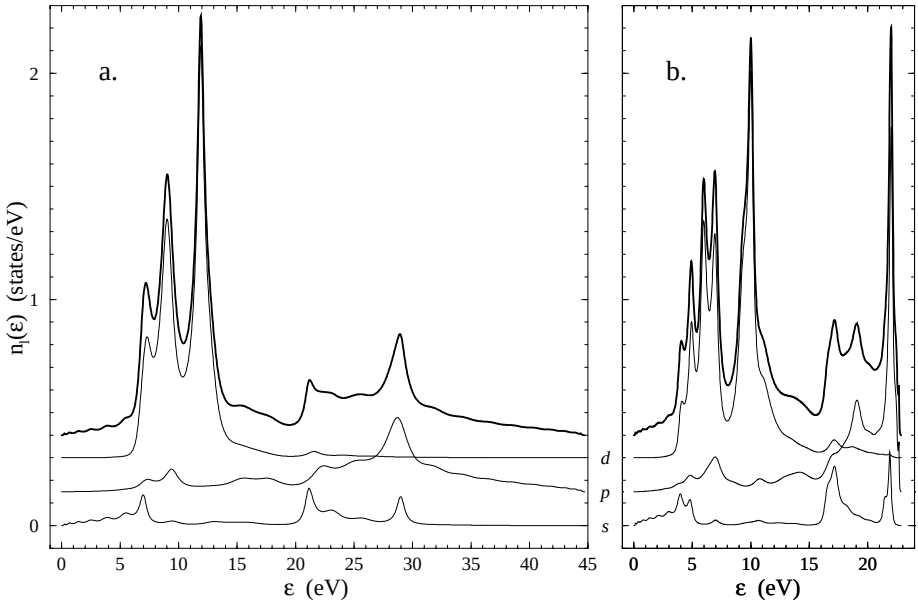

Fig. 1. *s*, *p*, *d* and total *(bold line)* densities of states obtained with 24 exact levels of the continuous fraction for bulk non magnetic Chromium with tight binding parameters taken from *a.* Papaconstantopoulos [9] and *b.* Andersen *et al* [10]

calculation (Fig. 1.a). It is then essential to choose tight binding parameters giving the smallest total band width in order to describe more precisely the *d* band of transition metals around the Fermi level. This is why, in the following, the tight binding parameters deduced by Andersen *et al* [10] are used.

2.3 Clusters for the Recursion Method

It has been shown previously that, for each additional level of the recursion fraction, the next shell of "neighbours" of the starting site $|0\}$ is taken into account. For the calculation of N_{exact} recursion levels, we have to built a cluster containing all sites which will contribute. This exact cluster correspond to all sites geometrically included in the N_{exact}-th shell of "neighbours". The shape of the exact cluster depends on the crystallographic structure and the cut-off r_c of the hopping integrals ($\beta_{i,j}^{\lambda,\mu} = 0$ when $|\mathbf{r}_i - \mathbf{r}_j| > r_c$) which can be approximated by a sphere centered on the starting site of radius $R = R^* = N_{\text{exact}}.r_c$ (this sphere contains the exact cluster). The number of sites N_{site} included in the sphere increases with N_{exact} like N_{exact}^3 and the computation time increases in the same way. This is why, in most cases smaller clusters are used. However, the recursion coefficients are affected by the size and the shape of these "inexact" clusters.

As an illustration, cubic and spherical "inexact" clusters are built and the

DOS obtained for various cluster sizes are compared. The minimal cubic cluster containing the exact cluster includes all sites i verifying $|x_i| < a/2$, $|y_i| < a/2$, $|z_i| < a/2$ with $a = a^* = 2N_{\text{exact}}.r_c$. "Inexact" clusters are built with a smaller radius for spheres or a smaller edge for cubes. They are defined by the ratio $\rho = R/R^*$ for spherical clusters and $\rho = a/a^*$ for cubic ones.

Tables 1 and 2 present some characteristics of such "inexact" clusters and Figs. 2 and 3 display the DOS obtained for two of these examples. These results (Tables 1 and 2) shows that, as expected, for a similar number of sites in the clusters, the number of exact levels obtained during the calculation of 24 levels, is larger for a spherical cluster than for a cubic one. However, the comparison with the exact calculation (Fig. 1.b) shows that the DOS (Figs. 2 and 3) obtained with spherical clusters exhibit more non physical peaks (mainly near the bottom of the DOS) than the others; these peaks are mostly found in the s band. This can be easily understood because the spherical cluster is a much better approximation of the exact cluster than a cube and consequently the missing sites correspond to complete shells whereas, for cubic cluster, they correspond to fractions of shells. During the calculation of successive levels, the missing sites have a more progressive impact when cubic clusters are used than with spherical ones for which the impact occurs abruptly at a given level. In this work, cubic clusters are used, in order to keep the cubic symmetry of the considered crystals, with $\rho = 0.25$ and the DOS are determined with 24 levels in the continuous fraction. Of course, for other crystals, other "inexact" (non spherical) clusters have to be consider.

The previous considerations on the cluster shape have been done for bulk

Table 1. Some examples of "inexact" cubic clusters for various ratio ρ. The number of exact recursion levels and the computation time required for calculating 24 levels are displayed; the cluster built with $\rho = 1$ contains the exact cluster needed for the calculation of 24 exact recursion levels

Linear scale ratio ρ	Number of atoms	Number of exact levels	Computation time (s)
0.167	855	5	16
0.25	3925	11	38
0.5	29449	24[a]	238
1	228241	24	6106

[a] differences between calculated and exact coefficients smaller than 10^{-10}.

situation for which there is only one non equivalent atom in the unit cell. For cells containing a large number of non equivalent sites, there are two possible ways to build an "inexact" cluster (Fig. 4): (i) building a set of cubic clusters centered on each non equivalent site or (ii) building an unique cluster by joining

Table 2. Some examples of "inexact" spherical clusters for various ratio ρ. The number of exact recursion levels and the computation time required for calculating 24 levels are displayed; the cluster built with $\rho = 1$ contains the exact cluster needed for the calculation of 24 exact recursion levels

Linear scale ratio ρ	Number of atoms	Number of exact levels	Computation time (s)
0.195	869	6	16
0.325	3942	15	40
0.635	29627	24[a]	250
1	115633	24	1556

[a] differences between calculated and exact coefficients smaller than 10^{-10}.

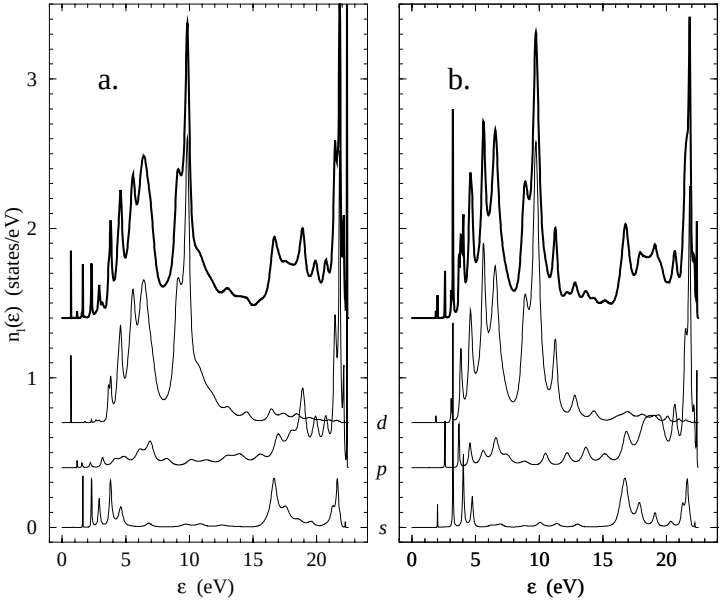

Fig. 2. *s*, *p*, *d* and total *(bold line)* densities of states obtained with 24 levels of the continuous fraction for bulk non magnetic Chromium for *a.* a cubic cluster with $\rho = 0.167$ and *b.* a spherical cluster with $\rho = 0.195$; both clusters contain approximately 850 sites

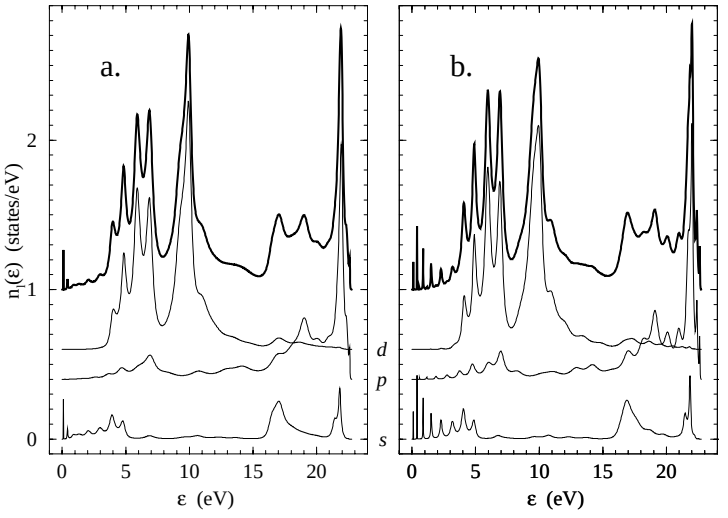

Fig. 3. *s*, *p*, *d* and total *(bold line)* densities of states obtained with 24 levels of the continuous fraction for bulk non magnetic Chromium for *a.* a cubic cluster with $\rho = 0.25$ and *b.* a spherical cluster with $\rho = 0.325$; both clusters contain approximately 3900 sites

together all clusters built previously. In the first construction, if the unit cell is longer than $a/2$, all non equivalent sites are not included in one cluster (Fig. 4.a). This is problematic when interactions between distant atoms are studied because one of the atoms is outside the cluster and no direct interactions are taken into account. The second cluster construction solves this problem by including all atoms of the unit cell in the cluster. However, this long cluster breaks the cubic symmetry and the different sites are no more equivalent from the point of view of the recursion calculation.

In order to have an idea of the fluctuations introduced by such a long cluster, the bulk antiferromagnetic Chromium situation is considered where all atoms are equivalent and the length n of the unit cell is artificially increased. With exact clusters, the result does not depend on the size of the cell. The results obtained with the "inexact" cluster are presented on Table 3. The local magnetic moment fluctuates only very slightly (fluctuations from site to site smaller than 10^{-5} μ_{B}) but it decreases when the unit cell is increased. The on-site energy shows more pronounced fluctuations from site to site. This shows clearly that the size and the shape of the cluster play an essential role on the calculated properties when the unit cell is varied. This is exactly what is usually done for multilayers where the properties are studied as a function of the layer thickness.

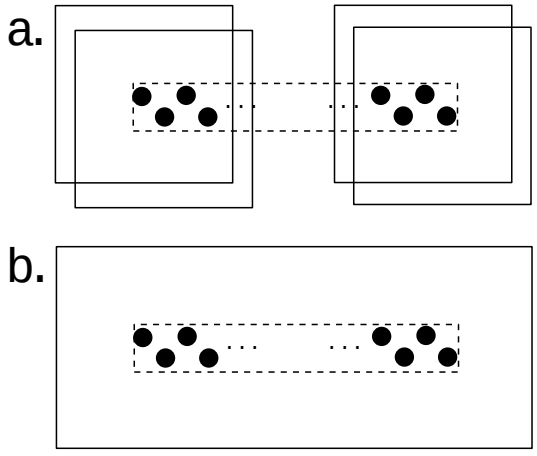

Fig. 4. Schematic representation of the two kind of clusters considered for long unit cells *(dashed line)* containing a large number of non equivalent sites *(filled circles)*: *a.* a set of cubic clusters centered on each non equivalent site are built, *b.* an unique cluster containing all clusters of the *(a)* situation is built

Table 3. Magnetic moment values (M) and energy on the sites i in the unit cell of length n which are not equivalent in the "inexact" unique cluster relative to the value obtained with a single atom in the unit cell $\Delta E(i) = E(i) - E(0,\ n = 1)$

	M (μ_B)	$\Delta E(0)$ (meV)	$\Delta E(1)$ (meV)	$\Delta E(2)$ (meV)	... ...
$n = 1$	0.6001	0			
$n = 2$	0.5868	−0.52			
$n = 3$	0.5796	−0.50	−0.69		
$n = 4$	0.5743	−0.68	−0.72		
$n = 5$	0.5731	−0.75	−0.75	−0.75	
$n = 6$	0.5727	−0.76	−0.76	−0.76	
$n = 11$	0.5725	−0.76	−0.76	−0.76	...

3 Periodic Versus Real Space Cells for Studying Bulk Magnetic Wall in Cr

The study of the Interlayer Magnetic Couplings (IMC) in Fe_mCr_n as a function of n requires the determination of the total energy from the electronic structure for various interlayer magnetic arrangement (IMA). Usually, they are restricted to collinear "ferromagnetic" (F) and "antiferromagnetic" (AF) IMA corresponding respectively to parallel and antiparallel magnetisation of successive Fe layers. The IMC are positive (respectively negative) as expected from the occurrence of a central magnetic defect in the Cr spacer when its thickness corresponds to an odd (even) number of atomic layers with an AF (F) interlayer arrangement [11]. For large spacer thickness, this defect becomes a bulk wall in the [001]

direction in a layered antiferromagnetic crystal. This bulk wall resembles to a Bloch wall in a ferromagnet separating two domains in the limit of a very strong anisotropy giving collinear magnetism. In the present case, the bulk wall in a antiferromagnet corresponds to an antiphase in the layered antiferromagnetic order. It is easy to build such magnetic configurations using periodic or real space cells. The periodic cell consists in a Cr_1Cr_{2n-1} superlattice with an AF interlayer arrangement between the Cr_1 layers (Fig. 5.a). The real space cell consists in a block of $2n-1$ atomic planes on which the wall is induced by a symmetry relative to the central atomic plane is applied (if this plane has a zero index, the symmetry corresponds to a magnetic moment on the i-th atomic plane given by $M_i = -M_{-i}$), this block being surrounded by blocks for which the magnetic moments are frozen in a AF bulk-like configuration (Fig. 5.b).

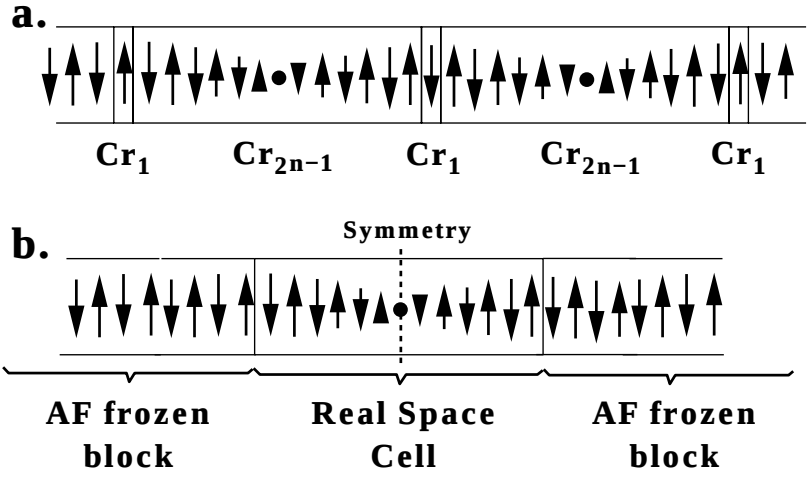

Fig. 5. Schematic representation of the cells used for calculating the bulk magnetic wall in AF Cr: *a.* a periodic cell built like a Cr_1Cr_{2n-1} superlattice with an AF interlayer arrangement, *b.* a real space cell, containing $2n-1$ atomic planes with a symmetry applied relative to the central atomic plane reversing the magnetic moments, surrounded by bulk-like frozen AF Cr blocks

The calculation of the magnetic structure using a periodic cell is similar to the one of Fe_mCr_n superlattices: the Fermi level E_F is given by the global neutrality requirement:

$$\sum_{i,l} \Delta N_{i,l} = 0. \tag{20}$$

With the real space cell, the situation is more complex because the two semi-infinite bulk-like frozen AF Cr blocks fix E_F to the bulk value. The local energy

levels $\epsilon_{i,l}$ are adjusted requiring the local neutrality:

$$\sum_{l} \Delta N_{i,l} = 0 \tag{21}$$

which is a reasonable approximation since the charge variations in transition metals are usually small.

In this section, the study is restricted to a *d* description, because for collinear magnetism, the results obtained with this band structure description are more than qualitatively correct [12]. The characteristics (extent and energy) of the AF bulk wall can be determined with both cells using large thickness. In this paragraph, by increasing n, the two approaches (periodic and real space) are compared and the minimal value for n, for which the characteristics of the bulk wall do no more change significantly, is determined. With a periodic cell, the criterion is to recover the bulk value of the magnetic moment on the Cr_1 atomic plane and, with the real space cell, it is to have a continuous behaviour at the frontier between the cell and the "frozen" blocks. Fig. 6 presents these values a function of n. The criterion is more rapidly satisfied with a real space cell than with a periodic one. Moreover, all magnetic moments are found equal to zero for periodic cells with $n < 9$ whereas with this value for n, 90 % of the bulk moment is reached with the real space cell. This result is not very surprising since, with the real space cell, the moment at the frontier between the cell and the "frozen" blocks is strongly maintained by the proximity of a frozen bulk magnetic moment on one side and only slightly reduced by the magnetic defect on the other side. For periodic cells, the magnetic defect cancels all moments in too small cells. This illustrates the efficiency of the use of real space cells for studying non interacting magnetic configurations.

Using the real space approach, the characteristics of the bulk collinear magnetic wall in Cr can now be investigated. The insert of Fig. 7 shows the magnetic moment profile of the wall: its extent is found approximately equal to 40 atomic planes. This shows that a frustration in the Cr AF order has repercussions over a large range of planes making this spacer particularly suited for studies with the present light approach since a large number of Cr atoms are concerned. Finally, the asymptotic limit of the energy of this wall as a function of n seems to be $\gamma_{Cr} = 21$ meV per in plane atom (Fig. 7). This energy corresponds to the energy of the interlayer couplings obtained for large Cr thickness demonstrating that the coupling energy does not decrease in the collinear restriction when the spacer thickness increases in such Fe/Cr superlattices.

4 Non-Collinear Magnetism

4.1 Continuous Fraction Expansion and Non-Collinear Magnetism

All studies presented in the previous section have been realized in the collinear magnetism framework which saves computer time but represents a strong limitation as compared to experiments. The band structure non-collinear magnetism

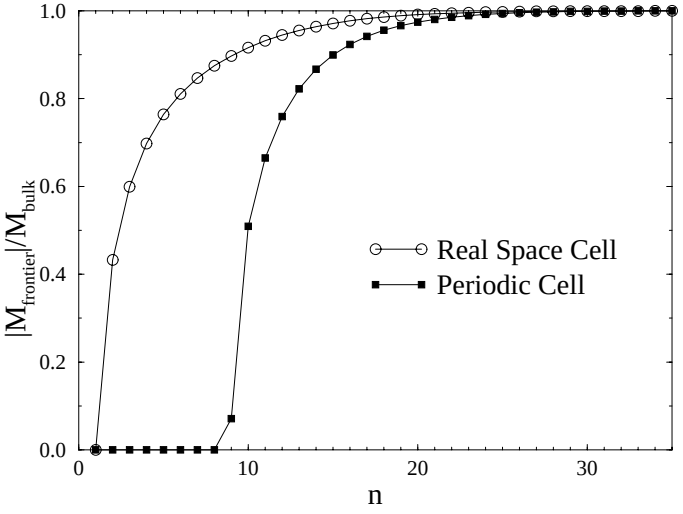

Fig. 6. Magnetic moments values relative to the bulk value on the Cr_1 atomic plane (*filled squares*) of the Cr_1Cr_{2n-1} periodic cell and on the atomic plane at the frontier between the cell and the "frozen" blocks (*open circles*)

allows to include the angular degree of freedom in the self consistent calculation [13,14]. The magnetic moment is a vector having 3 components M_x, M_y and M_z or can be described by its magnitude M_r and two spherical angles θ and ϕ. First, the input hamiltonian expression has to be modified in order to take into account the varying local spin quantization axis ζ_i (whose direction is given by the two usual spherical angles θ_i and ϕ_i) for each site i and, second, to determine the components $M_{r,i}$, $M_{\theta,i}$ and $M_{\phi,i}$ of the output magnetic moment.

The hamiltonian of (16) can be rewritten as a sum of a band H_{band} and an exchange H_{exch} hamiltonian where:

$$H_{\text{band}} = \left[\sum_{i,\lambda} |i,\lambda\rangle(\epsilon^0_{i,\lambda} + U_{i,l(\lambda)}\Delta N_{i,l(\lambda)})\langle i,\lambda| + \sum_{(i,\lambda)\ (j\neq i,\mu)} |i,\lambda\rangle\beta^{\lambda,\mu}_{i,j}\langle j,\mu| \right] \begin{pmatrix} 1 & 0 \\ 0 & 1 \end{pmatrix} \tag{22}$$

and

$$H_{\text{exch}} = \sum_{i,\lambda} |i,\lambda\rangle \frac{-I_{i,l(\lambda)}M_{i,l(\lambda)}}{2} \langle i,\lambda| \begin{pmatrix} \cos\theta_i & \mathrm{e}^{-\mathrm{i}\phi_i}\sin\theta_i \\ \mathrm{e}^{\mathrm{i}\phi_i}\sin\theta_i & -\cos\theta_i \end{pmatrix}. \tag{23}$$

In these expressions, the spin part of the hamiltonian is represented by the 2×2 matrix which is site dependent only in H_{exch}. Expression (23) is obtained by applying a rotation on the σ_z Pauli matrix in order to align the local quantization

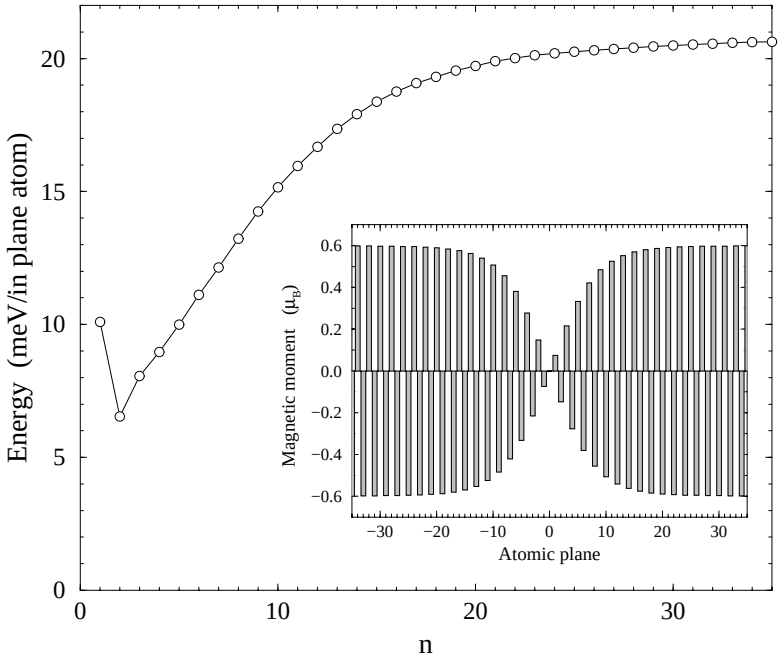

Fig. 7. Energy (in meV per in plane atom) of the bulk collinear magnetic wall as a function of the size n of the real space cell. The insert presents the magnetic moments profile of the wall

axis ζ_i with the global z axis.

The PDOS on site i for the symmetry λ is obtained with the recursion technique by setting the starting element $|0\rangle$ of the recursion basis equal to $|i,\lambda\rangle$. If the spin states are represented with the z quantization axis by a two elements vector, we have:

$$|i,\lambda,\sigma_\lambda=+\rangle=|i,\lambda'\rangle\begin{pmatrix}1\\0\end{pmatrix}\quad,\qquad|i,\lambda,\sigma_\lambda=-\rangle=|i,\lambda'\rangle\begin{pmatrix}0\\1\end{pmatrix}\tag{24}$$

where λ' corresponds to the symmetry of the spin symmetry λ. The PDOS on an arbitrary axis ζ defined by the two spherical angles (Θ,Φ) in the spin space is obtained by starting with the following initial recursion basis element:

$$\begin{aligned}|i,\lambda,\sigma_\lambda=+\rangle_\zeta&=|i,\lambda'\rangle\begin{pmatrix}\mathrm{e}^{-\mathrm{i}\Phi/2}\cos\frac{\Theta}{2}\\ \mathrm{e}^{-\mathrm{i}i\Phi/2}\sin\frac{\Theta}{2}\end{pmatrix}\\ |i,\lambda,\sigma_\lambda=-\rangle_\zeta&=|i,\lambda'\rangle\begin{pmatrix}-\mathrm{e}^{\mathrm{i}\Phi/2}\sin\frac{\Theta}{2}\\ \mathrm{e}^{\mathrm{i}\Phi/2}\cos\frac{\Theta}{2}\end{pmatrix}.\end{aligned}\tag{25}$$

For the determination of $M_{r,i}$, $M_{\theta,i}$ and $M_{\phi,i}$ using (19), the majority and minority spin states densities of states have to be calculated for all sites i and

symmetries λ' for $\zeta = \zeta_i$ aligned with $\mathbf{u}_{r,i}$ ($\Theta = \theta_i, \Phi = \phi_i$), for ζ aligned with $\mathbf{u}_{\theta,i}$ ($\Theta = \theta_i + \pi/2, \Phi = \phi_i$) and for ζ aligned with $\mathbf{u}_{\phi,i}$ ($\Theta = \pi/2, \Phi = \phi_i + \pi/2$).

The first step of the non-collinear study has been done using a d restricted

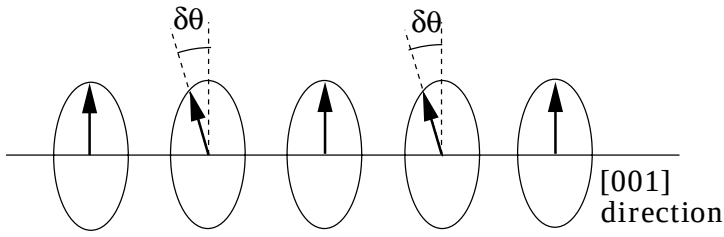

Fig. 8. Schematic representation of the slightly non-collinear magnetic configuration built by tilting the magnetic moment of one over two (001) atomic plane by a small angle $\delta\theta$

band structure description. In most cases studied, a discontinuous behaviour between collinear and slightly non-collinear calculations has been found. For example, a slightly non-collinear magnetic configuration by tilting the magnetic moment directions of half the (001) atomic planes by a small angle $\delta\theta$ is built as shown by Fig. 8. An antiferromagnetic order like in Cr is obtained for $\delta\theta = \pi$. When $\delta\theta$ is varied starting from zero (ferromagnetic order) and increased progressively, a nice continuous behaviour should be obtained. This is not obtained with a d band structure as shown by Fig. 9: the magnetic moment and the energy show rapid and large variations when $\delta\theta$ is varied from zero to 2°. On the contrary, the expected nice behaviour is obtained with a *spd* band structure as shown on the same figure. This peculiar behaviour comes from the not spin (+) and (−) mixed d densities of states in the ferromagnetic collinear configuration ($\delta\theta = 0$): the (+) and (−) d densities of states are determined completely independently from a calculation where all 2×2 matrices of (25) are diagonal. Since it is assumed that the tight binding parameters are not spin dependent, the (+) and (−) densities of states are the same (they have the same band width W and are only split in energy by $I_{i,d}M_{i,d}$) but they have different band limits (Fig. 10) and the (+) and (−) spin recursion coefficients $a_n^{i,\lambda}$ have different $a_\infty^{i,\lambda}$ limits:

$$a_\infty^{i,d,+} = \frac{\epsilon_{min}^{i,d,+} + \epsilon_{max}^{i,d,+}}{2} = a_\infty^{i,d,-} - I_{i,d}M_{i,d}$$
$$b_\infty^{i,d,+} = b_\infty^{i,d,-} = \left(\frac{W}{4}\right)^2 \tag{26}$$

When, the magnetic configuration is non-collinear (even slightly non-collinear), the (+) and (−) spin states are mixed and the (+) and (−) densities of states have the same band limits (this is not exactly the case in Fig. 10 because only 8 recursion levels are used but larger band widths are obtained) and the recursion

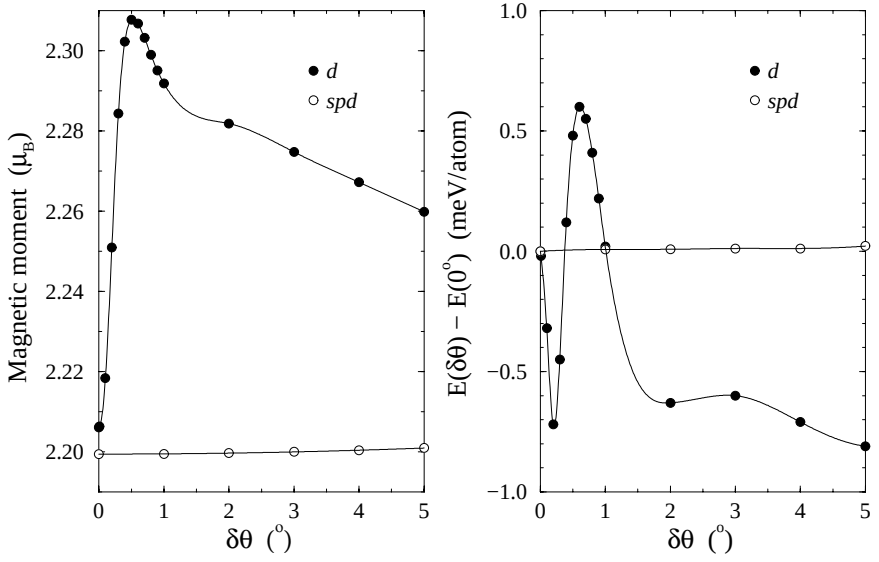

Fig. 9. Magnetic moments and energy variation as a function of the angle $\delta\theta$ of the magnetic configuration represented in Fig. 8 obtained with a *d* (*filled circles*) and with a *spd* (*open circles*) band structure

coefficients $(a_n^{i,\lambda}, b_n^{i,\lambda})$ should have the same $(a_\infty^{i,\lambda}, b_\infty^{i,\lambda})$ limit:

$$a_\infty^{i,d,+} = a_\infty^{i,d,-}$$
$$b_\infty^{i,d,+} = b_\infty^{i,d,-} = \left(\frac{W + I_{i,d}M_{i,d}}{4}\right)^2 . \tag{27}$$

This explains the large differences in the densities of states represented by Fig. 10. The most significant changes are mainly noticeable at the top of the majority spin band where a large peak occurs around one eV even for a very small $\delta\theta$ value. Such an unphysical behaviour is of course not obtained with an *spd* hamiltonian. In this case, the *d* band which carries the magnetism is hybridised with the *s* and *p* bands having a large band width and consequently the recursion coefficients limits $a_\infty^{i,\lambda}$ are nearly insensitive to changes in the magnetic configuration.

For non-collinear studies, a restricted *d* hamiltonian has to be used very carefully in order to avoid unphysical results related to numerical problems in the continuous fraction expansion. All these problems are nicely solved when a *spd* hamiltonian is used.

4.2 Angular Dependence of the Interlayer Magnetic Couplings in Fe/Cr Multilayers

The interlayer magnetic couplings discussed previously can now be studied in the non-collinear framework and their angular dependence can be investigated.

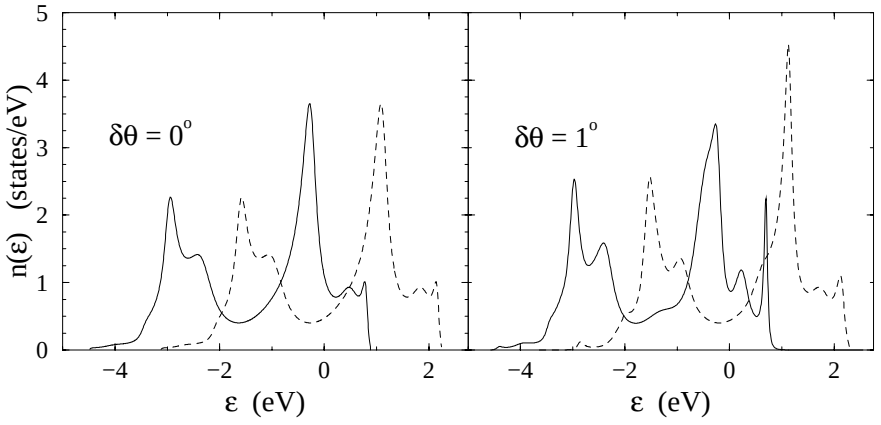

Fig. 10. Densities of states for bulk Fe obtained considering the magnetic configuration of Fig. 8 with $\delta\theta = 0°$ (ferromagnetic order) and $\delta\theta = 1°$ (slightly non-collinear order). The majority (respectively minority) spin bands are represented by solid (dashed) lines

This is done by fixing the angle $\Delta\theta$ between the directions of the inner magnetic moments of successive ferromagnetic layers during the self-consistent calculation as displayed by Fig. 11. During the calculation, all not fixed magnetic moments

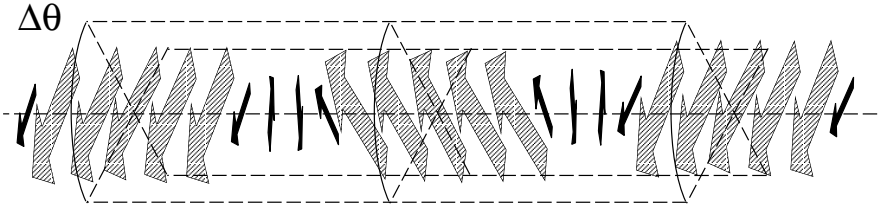

Fig. 11. Schematic representation of the magnetic configuration considered for the calculation of the interlayer magnetic couplings. Each vector corresponds to the magnetic moment of all atoms in the (001) atomic plane which are equivalent

are free to rotate and self-consistency is assumed to be achieved when the output perpendicular components $M_{\theta,i}$ and $M_{\phi,i}$ on all these sites i are nearly equal to zero. In this paper, the angular variation is restricted to θ in order to reduce the computer time but also because it has been checked that all magnetic moments vectors are in the plane defined by the two fixed magnetic moments.

Because the d states are the most essential for the magnetism, the effective exchange integrals I_s and I_p are usually equal to zero. However, if this is usually arbitrarily assumed, setting $I_s = I_p = 0$ is now required because we obtain self-consistency by an iterative way for non-collinear solutions. This comes from the

expression of the output magnetic moment in terms of s, p and d contributions in the input $\mathbf{u}_{i,r}^{(\text{in})}$ and $\mathbf{u}_{i,\theta}^{(\text{in})}$ spherical basis:

$$\begin{aligned} M_{i,r}^{(\text{out})} &= M_{i,r,s}^{(\text{out})} + M_{i,r,p}^{(\text{out})} + M_{i,r,d}^{(\text{out})} \\ M_{i,\theta}^{(\text{out})} &= M_{i,\theta,s}^{(\text{out})} + M_{i,\theta,p}^{(\text{out})} + M_{i,\theta,d}^{(\text{out})} \\ \mathbf{M}_{i}^{(\text{out})} &= M_{i,r}^{(\text{out})}\mathbf{u}_{i,r}^{(\text{in})} + M_{i,\theta}^{(\text{out})}\mathbf{u}_{i,\theta}^{(\text{in})}. \end{aligned} \tag{28}$$

The magnetic moment used as input for the next iteration is obtained by varying θ_i in order to align the local quantization axis with the direction of the output magnetic moment given by:

$$\begin{aligned} \mathbf{M}_{i}^{(\text{next in})} &= M_{i,r}^{(\text{next in})}\mathbf{u}_{i,r}^{(\text{out})} \\ &= \mathbf{M}_{i}^{(\text{out})} \end{aligned} \tag{29}$$

in the output $\mathbf{u}_{i,r}^{(\text{out})}$ and $\mathbf{u}_{i,\theta}^{(\text{out})}$ spherical basis. The s, p and d decomposition of the next input magnetic moment has to be obtained:

$$M_{i,r}^{(\text{next in})} = M_{i,r,s}^{(\text{next in})} + M_{i,r,p}^{(\text{next in})} + M_{i,r,d}^{(\text{next in})} \tag{30}$$

which is equal to the magnitude of the output magnetic moment vector

$$\sqrt{(M_{i,r,s}^{(\text{out})} + M_{i,r,p}^{(\text{out})} + M_{i,r,d}^{(\text{out})})^2 + (M_{i,\theta,s}^{(\text{out})} + M_{i,\theta,p}^{(\text{out})} + M_{i,\theta,d}^{(\text{out})})^2}. \tag{31}$$

However, this s, p and d decomposition is lost when the magnitude of $\mathbf{M}_{i}^{(\text{out})}$ given by (31) is calculated. If $I_s = I_p = 0$, the results are the same whatever the values of $M_{i,r,s}^{(\text{in})}$ and $M_{i,r,p}^{(\text{in})}$ are (they do not contribute to the exchange field) and we have to do the self-consistent calculation only for the d component of the magnetic moments:

$$M_{i,r,d}^{(\text{next in})} = \sqrt{(M_{i,r,d}^{(\text{out})})^2 + (M_{i,\theta,d}^{(\text{out})})^2}. \tag{32}$$

The calculation is assumed to be converged when

$$\begin{aligned} \text{Max}_i\{|M_{i,r,d}^{(\text{out})} - M_{i,r,d}^{(\text{in})}|\} &< \epsilon \\ \text{Max}_i\{|M_{i,\theta,d}^{(\text{out})}|\} &< \epsilon \\ \text{Max}_i\{|E_{\text{tot}}^{(\text{out})} - E_{\text{tot}}^{(\text{in})}|\} &< \epsilon' \end{aligned} \tag{33}$$

with $\epsilon = 5 \times 10^{-5}$ μ_{B} and $\epsilon' = 10^{-5}$ eV.

Fig. 12 presents the interlayer magnetic couplings obtained with the d and the two *spd* tight binding parameters as a function of $\Delta\theta$ for Fe_5Cr_4 and Fe_5Cr_5 superlattices. Around the energy minimum, the coupling energy follows a parabolic expression $C_+(\Delta\theta - \pi)^2$ for $n = 4$ and $C_+(\Delta\theta)^2$ for $n = 5$ as predicted by a phenomenological model [15]. The couplings obtained with the d tight binding

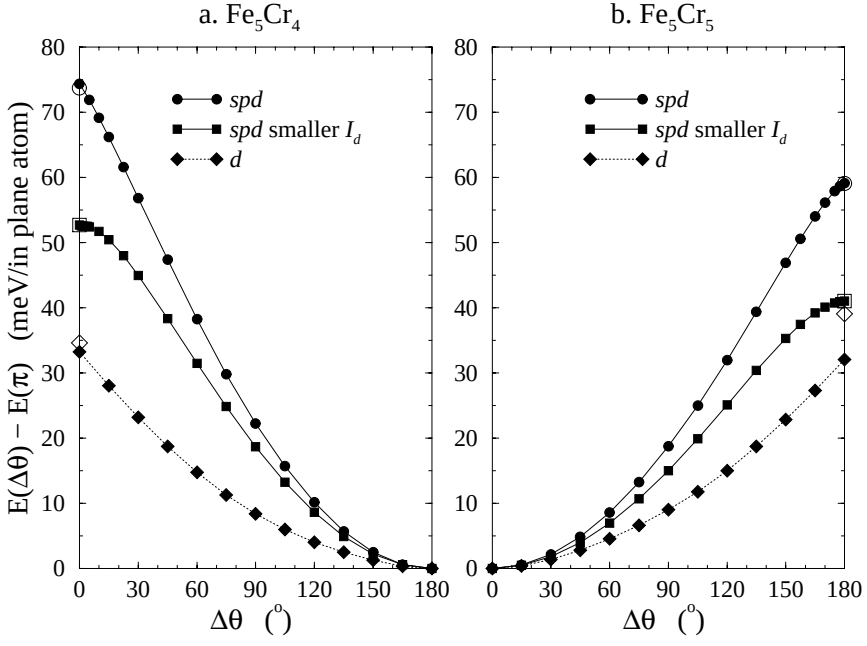

Fig. 12. Interlayer magnetic couplings $\Delta E(\Delta\theta) - E(\pi \text{ or } 0)$ obtained with the d (*filled diamonds*) and the *spd* tight binding parameters without (*filled circles*) and with (*filled squares*) a smaller interfacial I_d as a function of $\Delta\theta$ for Fe_5Cr_4 and Fe_5Cr_5 superlattices. The open symbols correspond to the collinear solution

parameters follow the parabolic function over the whole range of $\Delta\theta$ considered. The collinear solution obtained for the frustrated configuration does not correspond to the solution obtained for $\Delta\theta = 0$ ($n = 4$) and π ($n = 5$) and has a higher energy. This is not very surprising since, with these parameters, the Fe and Cr magnetic moments do not vary significantly when $\Delta\theta$ varies and the local angles θ_i vary nearly linearly with $\Delta\theta$ as previously reported [16]. Such a *nearly constant magnetic moment magnitude* behaviour corresponds exactly to the phenomenological model which assumes a helical configuration in a Heisenberg model for the antiferromagnetic spacer. The behaviour of the coupling energies for *spd* tight binding parameters is completely different: they follow the parabolic function only over half the range of $\Delta\theta$ considered. This is particularly pronounced when the interfacial Cr I_d is reduced from 0.96 eV to 0.90 eV (in order to have a better agreement with *ab initio* calculations) where the coupling energies show a maximum at $\Delta\theta = 0$ ($n = 4$) and π ($n = 5$). Moreover, the frustrated collinear solution energies are nearly degenerate with the ones of the corresponding solution obtained with the non-collinear calculations. For example, for Fe_5Cr_4 superlattices, during the decrease of $\Delta\theta$ from π to 0 (i) the Fe magnetic moments have a nearly constant magnitude (ii) the magnitude of the magnetic moments on the Cr atoms decreases strongly when $\Delta\theta$ reaches 0 and

the magnetic moment of the central Cr atomic planes nearly vanishes, (iii) the local angles vary linearly when $\Delta\theta$ decreases from 180° down to approximately 60°; for smaller $\Delta\theta$ values they vary very rapidly and reach values corresponding to the frustrated collinear magnetic configuration for $\Delta\theta = 0$.

This result explains qualitatively the different behaviours experimentally obtained for FeCo/Mn superlattices where the parabolic function applies [17] and for Fe/Cr superlattices where the saturation is better reproduced with a $J_1.\cos(\Delta\theta) + J_2.\cos^2(\Delta\theta)$ expression for the coupling energy [18].

4.3 Step Induced Non-Collinear Magnetism

In the previous paragraph, the non-collinear character is induced by the variation of $\Delta\theta$. This is similar, for $n = 4$, to the situation where an increasing external magnetic field is applied on the multilayer. Non-collinear magnetic configurations can also be obtained when interfacial imperfections frustrate the natural magnetic order in the multilayer.

This is illustrated by Fig. 13 for interfacial atomic steps. Because Cr is an-

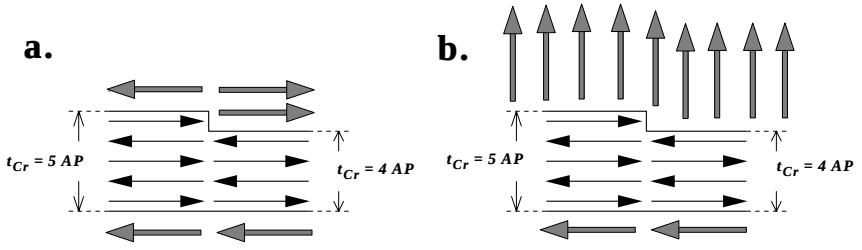

Fig. 13. Schematic representation of the frustration induced by an interfacial atomic step in an Fe/Cr/Fe sandwich: the Cr thickness t_{Cr} variation from 4 to 5 atomic planes (AP) *a.* splits the second Fe layer into domains of opposite magnetisation when the interfacial coupling is preserved or *b.* induces a 90° interlayer arrangement when the interfacial coupling is partially frustrated

tiferromagnetic, the sign of the interfacial Cr magnetic moment changes from one (001) atomic plane to the next. If the antiparallel interfacial Fe-Cr coupling and the Cr antiferromagnetic order (for small Cr thickness) are preserved, the interlayer magnetic coupling changes from AF to F when the Cr thickness t_{Cr} varies from $n = 4$ to $n = 5$ atomic planes at the atomic step (Fig. 13.a). The second Fe layer is then split into domains of opposite magnetisation and the domain walls correspond to the steps [19]. However, if we allow non-collinear magnetism, the second Fe layer can be nearly monodomain if its magnetisation is perpendicular to the one of the first Fe layer as shown by Fig. 13.b where we have assumed that only the interfacial Fe-Cr coupling is partially frustrated. This behaviour, resulting from the competition between the strong Fe ferromagnetism and the fluctuations of the interlayer coupling, is usually invoked for explaining

the occurrence of 90° interlayer arrangements but does not result from an intrinsic biquadratic interlayer coupling. The aim of this part is to use our method to determine explicitly the magnetic moment map for such configurations.

For these calculations, all magnetic moments are free to rotate until self-consistency is achieved. However, because we do not include the spin-orbit coupling, a global rotation can be applied on all moments without changing the solution (there are no privileged directions for the magnetisation). Consequently, when all moments are effectively free to rotate, the calculation can never converge because a global rotation can occur during each iteration and θ_i can never reach its asymptotic value. Fixing arbitrary one moment (on site 0 for example) and allowing all others to rotate is not the best way to obtain the self-consistent map: the torque applied on the fixed site by all other sites is usually very large and a large number of iterations is needed in order to reduce significantly $M_{0,\theta,d}$ and to satisfy the convergence criteria (33) on all sites. A better way is to applied a global rotation at each iteration in order to keep the moment on a given site (the site 0) fixed in direction. The value for θ_i at the next input is then

$$\theta_i^{(\text{next in})} = \theta_i^{(\text{out})} - \theta_0^{(\text{out})} \tag{34}$$

and the angular self-consistency is obtained when

$$\text{Max}_i\{|M_{i,\theta,d}^{(\text{out})} - M_{i,r,d}^{(\text{out})}.\theta_0^{(\text{out})}|\} < \epsilon. \tag{35}$$

In this case, the final map is obtained when the magnetic moments do no more rotate relatively each others even if they continue to rotate globally from one iteration to the next.

Superlattices with atomic steps at one Fe/Cr interface like in Fig. 13 are modelled by periodic superlattices having a perfectly flat Fe layer separated from a rough second Fe layer by the Cr spacer with varying thickness. In the cases considered in this paper, *i.e.* atomic steps along the [010] direction with flat terraces having all the same size of 5 atomic rows, the cell corresponds to the lateral juxtaposition of 5 $Fe_5/Cr_5/Fe_5/Cr_5$ and 5 $Fe_5/Cr_4/Fe_7/Cr_4$ cells (see Fig. 14). The total real space cell contains 110 non equivalent sites. The calculations have been done using the *d* restricted parameters and the two sets of *spd* parameters previously used. The magnetic moment map obtained with the *d* restricted parameters of Fig. 14 shows clearly that (i) the rough Fe layer is structured in domains of opposite magnetisation corresponding exactly to the terraces, (ii) only the Fe atoms at the border line of the domains have a local magnetic moment perpendicular to the others, and (iii) the Cr spacer layer displays only a slight non-collinear character. This result does not correspond to the expected 90° interlayer arrangement and presents a strongly reduced magnetisation of the 'rough' Fe layer. On the contrary, with the *spd* parameters, the 'rough' Fe layer is (i) only slightly structured in magnetic domains having their magnetisation making an angle of approximately 80° and not 180°, (ii) the Cr spacer layer presents a more pronounced non-collinear character, and (iii) the magnetisation of the 'rough' layer, which is only slightly reduced, is preferentially perpendicular to the one of the flat Fe layer. The two sets of *spd* parameters used in this work

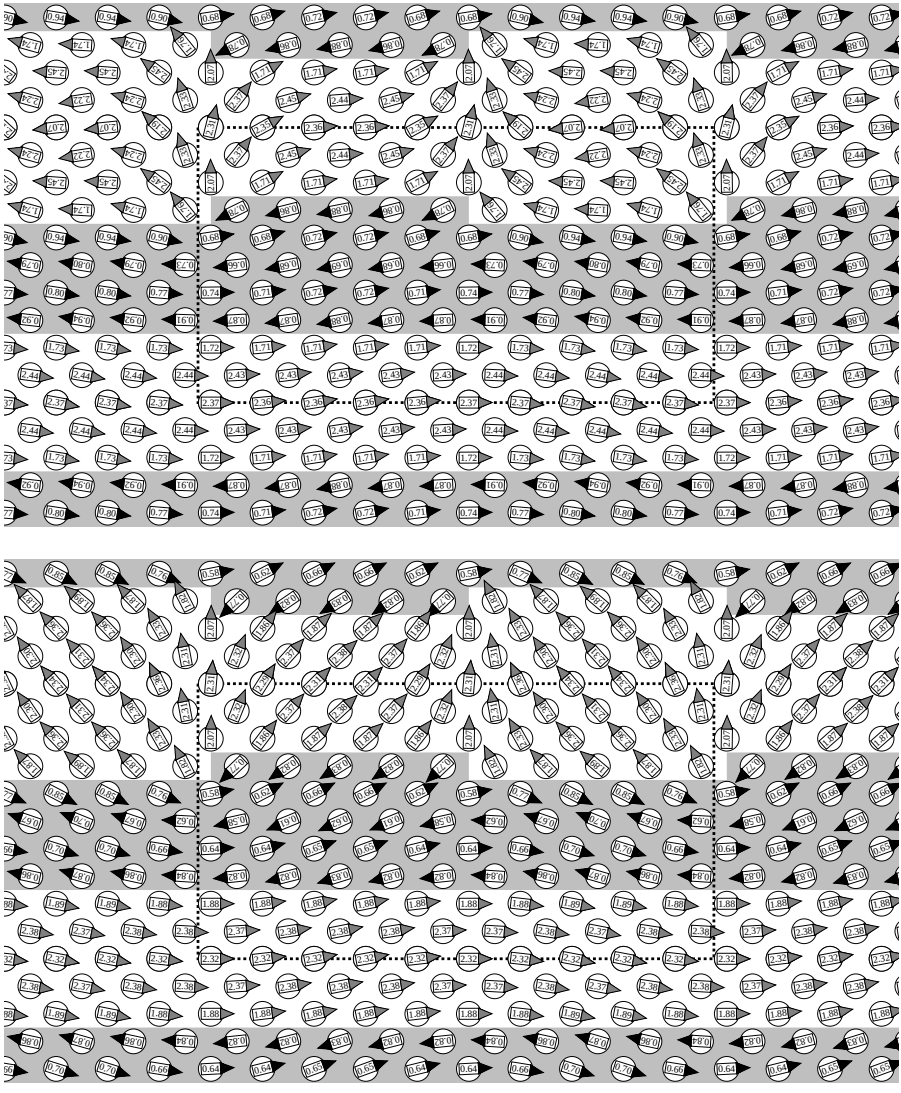

Fig. 14. Magnetic moment maps of a $Fe_{5.5}Cr_{4.5}$ superlattice having a perfectly flat 5 atomic planes thick Fe layer (*bottom layer*) and a rough Fe layer whose thickness varies from 5 to 7 atomic planes (*top layer*) separated by a Cr spacer layer whose thickness varies from 4 to 5 atomic planes obtained with the d restricted parameters (upper map) and with the *spd* parameters and the reduced Cr interfacial I_d (lower map). The arrow gives the direction of the local magnetic moment whose magnitude is given. The Fe sites have a grey arrow head and the Cr sites have a black one and a grey background

give nearly the same result. This behaviour corresponds more to the expected one.

5 Summary

It has been shown that real space methods like the recursion technique allow to study the magnetic properties of complex systems in a much larger variety of configurations than most of the other approaches. However, the use of a tight binding description of the band structure limits the confidence in the results and it has been exhibited that *d* restricted and *spd* parameters give significantly different results when non-collinear magnetic solutions are allowed. This is why, more accurate band structure description consistent with a real space approach are needed and the TB-LMTO method is a possible candidate.

Acknowledgements: The calculations presented in this work have been realized using facilities at the Institut de Physique et Chimie des Matériaux de Strasbourg, on the T3E parallel computer at the Institut du Développement et des Ressources en Informatique Scientifique (IDRIS) of the CNRS, on the SP2 parallel computer of the Centre National Universitaire Sud de Calcul (CNUSC) and on the parallel computer Origin 2000 at the Institut du Calcul Parallèle de Strasbourg (ICPS) of the Université Louis Pasteur. The authors acknowledge the TMR 'Interface Magnetism' Network (contract FMR-CT96-0089) for support.

References

1. R. Haydock, V. Heine, and M.J. Kelly, Journal of Physic C **5**, 2845 (1972).
2. R. Haydock, in Springer Series in Solid-State Sciences *The Recursion Method and Its Applications* published by Springer-Verlag (Berlin) **58**, 8 (1985).
3. V. Heine, in NATO ASI Series B: Physics *The Electronic Structure of Complex Systems* published by Plenum Press (New York) **113**, 761 (1984).
4. N. Beer, and D.G. Pettifor, in NATO ASI Series B: Physics *The Electronic Structure of Complex Systems* published by Plenum Press (New York) **113**, 769 (1984).
5. H. Dreyssé, and R. Riedinger, J. Physique **48**, 915-920 (1987).
6. R. Riedinger, M. Habar, L. Stauffer, and Dreyssé H., Léonard P., Nath Mukherjee M., Phys. Rev. B **39**, 2442 (1989).
7. J.C. Slater, and G.F. Koster, Physical Review **94**, 1498 (1954).
8. for example see in MRS Symp. Proc. **491** (1998).
9. Papaconstantopoulos D. A., *Handbook of the Band Structure of Elemental Solids* published by Plenum Press (New York) (1986).
10. O.K. Andersen, O. Jepsen, and D. Gloetzel, in *Highlights of Condensed Matter Theory* edited by Bassani F., Fumi F., Tosi M. P. published by North Holland (Amsterdam), page 59 (1985).
11. D. Stoeffler, and F. Gautier, Progress of Theoretical Physics, Supplement No. **101**, 139 (1990).
12. D. Stoeffler, and F. Gautier, J. Magn. Magn. Mater. **147**, 260 (1995).

13. D. Stoeffler, and C. Cornea, Computational Materials Science **10**, 217 (1998).
14. C. Cornea, and D. Stoeffler, Computational Materials Science **10**, 245; 249 (1998).
15. J.C. Slonczewski, J. Magn. Magn. Mater. **150**, 13 (1995).
16. M. Freyss, D. Stoeffler, and H. Dreyssé, Phys. Rev. B **54**, 12677 (1996).
17. M.E. Filipowski, J.J. Krebs, G.A. Prinz, and C.J. Gutierrez, Physical Review Letters **75**, 1847 (1995).
18. B. Heinrich *et al*, J. Magn. Magn. Mater., **140-144**, 545 (1995).
19. D. Stoeffler, F. Gautier, J. Magn. Magn. Mater. **156**, 114-116 (1996).